Research Square

Preprints are preliminary reports that have not undergone peer review.
They should not be considered conclusive, used to inform clinical practice,
or referenced by the media as validated information.

State-insensitive optical conveyor belts on integrated nanophotonic waveguides

Henry Putley
University of Birmingham
Paul Griffin
University of Strathclyde
Marc Sorel
University of Glasgow
Douglas Paul
University of Glasgow
Angela Demetriadou
a.demetriadou@bham.ac.uk

University of Birmingham

Article

Keywords:

Posted Date: November 19th, 2026

DOI: https://doi.org/10.21203/rs.3.rs-10315686/v1

License: This work is licensed under a Creative Commons Attribution 4.0 International License.
Read Full License

Additional Declarations: No competing interests reported.

State-insensitive optical conveyor belts on integrated nanophotonic waveguides

H.J. Putley,[1] P.F. Griffin,[2] M. Sorel,[3] D.J. Paul,[3] and A. Demetriadou[1,*]

[1]*School of Physics and Astronomy, University of Birmingham, B15 2TT Birmingham, UK*

[2]*SUPA and Department of Physics, University of Strathclyde, G4 0NG Glasgow, UK*

[3]*James Watt School of Engineering, University of Glasgow, Rankine Building, Oakfield Avenue, Glasgow, G12 8LT, UK*

(Dated: July 10, 2026)

Abstract

Integrated atom-nanophotonic platforms offer a promising route towards on-chip quantum technologies by enabling strong light–matter interactions in compact geometries. Here, we propose a *state-insensitive* optical conveyor belt for cold cesium (Cs) atoms along an integrated nanophotonic waveguide. Using a magic compensation scheme and appropriate frequency ramping, we achieve deep phase-matched confinement in the moving frame of atoms in both their ground and excited states pertaining to their D_2 transition. This conveyor effect allows for the coherence-preserving transport of atomic ensembles over micrometer-scale distances, as well as the acceleration and injection of atoms into a flat, atom guide potential, which is independent of their internal state. This work paves the way for controlled atom transport and state-insensitive manipulations in integrated nanophotonic architectures, for on-chip quantum information processing and matter wave inertial sensing.

I. INTRODUCTION

Recent advances in nanofabrication and integrated photonics have allowed for the optical trapping of cold atoms using photonic nanostructures, facilitating the translation of a range of lab-based atomic systems to compact, on-chip architectures. Emerging platforms include atomtronic [1–3], atomic [4] and coherent matter wave [5] circuits, among others [6]. An atom-nanowaveguide system leverages the nanostructure's eigenmodes (which carry a significant fraction of their total energy in a tightly confined evanescent field) to trap cold atoms, usually within ~ 400 nm of the nanostructure surface. Atoms are typically trapped by the combined optical potentials of multiple guided modes, confined in two- or three-dimensions with long trap lifetimes. The most widely studied realizations are tapered optical nanofibers, which have been shown to provide an excellent platform for the trapping [7–9], micromanipulation [10, 11] and interrogation [12–15] of cold atoms. Such capabilities are also available to integrated atom-nanowaveguide systems, which typically comprise of silicon-based nanoscopic components on-chip. These are emerging as a test-bed for chip-scale matter wave interferometers [4–6, 16], quantum sensing [17, 18] and quantum information processing [19], and may form the general architecture to underpin quantum computers [20].

* Corresponding author: a.demetriadou@bham.ac.uk

However, a key challenge in trapping cold atoms with nanostructures is the strong state-dependency of the spatially varying optical potential. This arises due to the significant ellipticity in polarization of the (non-paraxial) nanostructure eigenmodes throughout the evanescent region [17], which acts as a fictitious magnetic field and leads to a Zeeman broadening in the atomic level shifts [21, 22]. This limits both the trap lifetime and spin-wave coherence time, since an atomic ensemble experiences rapid dephasing whilst in such an optical trap [12]. This can be remedied by employing a *state-insensitive* trapping potential, engineered such that select electronic states experience near-identical optical potentials [8, 14, 23, 24], an example of which is the 'magic compensated' trapping scheme [12, 13]. To compensate for the elliptical polarization of a forward-propagating eigenmode, a backward-propagating eigenmode can also be introduced to cancel the ellipticity-induced Zeeman broadening. The resulting optical trapping potential is effectively insensitive to all ground and excited state atomic sublevels.

The optical transport of cold atoms by light, known as the optical conveyor effect [25, 26], is an effective tool for the micromanipulation of atoms in nanophotonic environments, enabling the assembly of atom arrays [27], the lifting of atoms into and out of an optical lattice [17], and the delivery of atoms from an atom cloud onto a nanophotonic circuit [28]. With regards to nanostructures, the optical conveyor effect has so far been demonstrated along a tapered optical nanofiber [10], and shares similarities with the optical tractor beam effect [11] on the same platform. In these realizations, controlled atomic transport is achieved through the translation of a standing wave or beat potential along the nanofiber axis, with atoms trapped at the potential minima moving at a velocity set by the mutual detuning of the carrier eigenmodes. Such conveyor schemes have not yet been realized in fully integrated nanophotonic waveguide platforms, and the existing studies concerning nanofibers [10, 11] considered only the optical transport of ground state atoms. The remaining challenge then is to realize state-insensitive conveyor belts for cold atoms, suitable for integrated nanowaveguides and on-chip architectures.

Here, we conceptualize a 'magic optical conveyor belt' along an integrated nanowaveguide for the state-insensitive transport of cold atoms. We apply the 'magic compensated' trapping scheme to a ridge waveguide geometry and design a state-insensitive optical lattice for Cs atoms in the $6S_{1/2}$ and $6P_{3/2}$ manifolds. The optical lattice is translated along the waveguide axis using standard frequency detuning techniques for the red-detuned eigenmodes, consti-

tuting a conveyor effect. Use of magic wavelengths enables probing of the trapped atoms at the D_2 transition frequency without risking their loss from the conveyor belt, as the trapping potential of the $6P_{3/2}$ state is of a similar amplitude to, and moves in-phase with, the potential of the $6S_{1/2}$ state. We propose that this magic conveyor effect offers a coherent transport mechanism for atomic ensembles across nanophotonic environments. Atoms can be moved deterministically along a nanowaveguide whilst preserving collective spin-wave coherence, enabling delivery to different interaction regions for quantum operations, or to state-selective light-atom interfaces. Finally, we also demonstrate how frequency and intensity ramping of the conveyor potential can be leveraged to accelerate atoms to a target velocity before releasing them into a smooth, state-insensitive 'atom guide' potential. An accelerator effect like this could see applications towards atom interferometry on integrated nanophotonic platforms [29]. The scheme also addresses a central requirement of atom-nanophotonic devices: preserving coherence during transport to strong-coupling regions of an integrated nanophotonic circuit. By conceptualizing a scalable, on-chip route to this kind of state-insensitive manipulation, our work complements ongoing efforts to integrate cold-atoms with nanophotonic quantum hardware [30].

II. RESULTS

A. ac Stark shift and surface interaction

We consider a general cold alkali atom in the vicinity of a nanowaveguide, optically trapped by the evanescent fields of a pair of waveguide eigenmodes red- and blue-detuned with respect to the atomic D lines. For an atom located within the two-color evanescent field, the total interaction Hamiltonian

$$H^{\mathrm{int}} = V^{\mathrm{hfs}} + V^{\mathrm{ls}} + V^{\mathrm{surf}} \tag{1}$$

is the sum of the hyperfine structure (hfs) interaction V^{hfs}, the ac Stark interaction – or *light shift* – V^{ls}, and the surface-interaction V^{surf} operators. The hfs interaction, which describes the coupling of the nuclear spin $\mathbf{I}$ to the total electronic angular momentum $\mathbf{J}$ (with quantum number J), provides the natural hfs basis $\{|nJFM\rangle\}$ of the atomic states in the absence of external fields. Here, F is the quantum number for the total angular momentum $\mathbf{F} = \mathbf{I} + \mathbf{J}$, M the quantum number for the projection of $\mathbf{F}$ onto the quantization axis, and n the set of

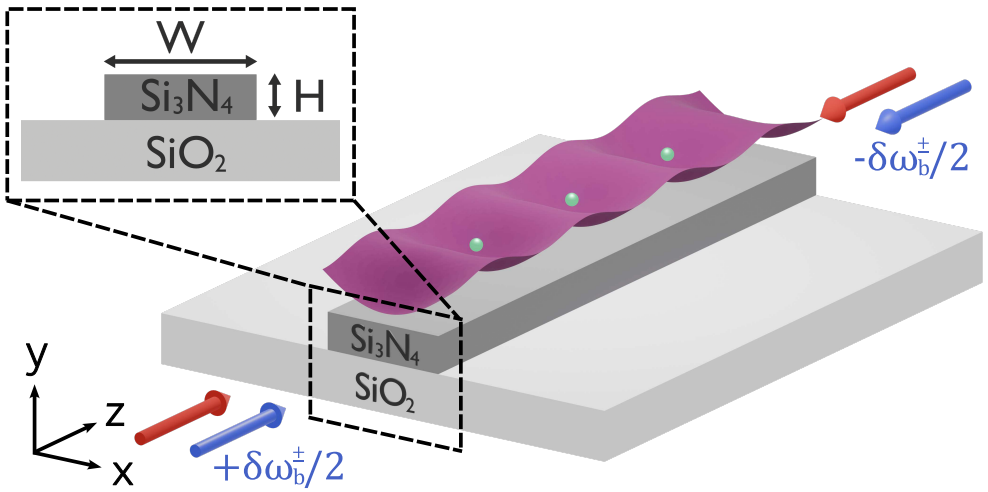


FIG. 1. Ridge optical waveguide and two-color trapping scheme. A ridge of Si_3N_4 atop a cladding of SiO_2 in vacuum. Counter-propagating red-detuned modes (red arrows) interfere to form a standing wave, corrugating the attractive potential along the waveguide axis, while two blue-detuned modes (blue arrows) supply the repulsive potential. The blue modes are also detuned from each other by a two-photon detuning $\delta\omega_b^{\pm}$. The combination of attractive and repulsive potentials forms an optical lattice, within which atoms (spheres) are trapped at the antinodes along the axial direction. The inset shows the waveguide cross-section.

remaining quantum numbers. As $V^{\rm hfs}$ is diagonal in the hfs basis, there is no mixing between hfs states and both F and M can be treated as good quantum numbers in the absence of external fields.

In general, the presence of an optical field ensures that neither F nor M are conserved, as the light shift operator $V^{\rm ls}$ couples different Zeeman sublevels and hyperfine states. However, when the light shift is small with respect to the hfs interaction, such as in far-off resonance optical traps, the mixing between different hyperfine levels $|nJF\rangle$ can be neglected, and the operator $V^{\rm hfs}$ can be omitted from the Hamiltonian. In this regime, F remains a good quantum number, and the total interaction Hamiltonian for an atom in the hyperfine state $|nJF\rangle$ reduces to

$$\bar{H}^{\rm int} = V^{\rm ls} + V^{\rm surf} \tag{2}$$

This Hamiltonian is expressed in the atomic hfs basis $\{|(nJF)M\rangle\}$ where parentheses indicate the now fixed quantum numbers nJF, and M denotes the Zeeman sublevels to the hfs level F.

1. Light shift potential

The operator V^{ls} governs the interaction between a multilevel atom and a classical light field [21, 31, 32]. We provide here the essential steps to its semi-classical description assuming a monochromatic field, but treat the bichromatic case in the Supplementary Information. A far-off resonance light field interacting with an atom gives rise to energy shifts of the atom's internal electronic states, collectively known as the ac Stark shift or light shift. This light shift acts as an adiabatic potential proportional to the local optical intensity and depends on the atomic polarizability, which in general contains scalar, vector, and tensor contributions. Consider a classical optical field of arbitrary polarization whose electric component $\mathbf{E}(\mathbf{r}, t)$ can be written

$$\mathbf{E} = \frac{1}{2}\boldsymbol{\mathcal{E}} e^{-i\omega t} + \text{c.c.} = \frac{1}{2}\mathcal{E}\hat{\mathbf{u}} e^{-i\omega t} + \text{c.c.} \tag{3}$$

where ω is the angular frequency, $\boldsymbol{\mathcal{E}} \equiv \boldsymbol{\mathcal{E}}(\mathbf{r}) = \mathcal{E}\hat{\mathbf{u}}$ is the positive-frequency electric field envelope, $\mathcal{E}$ is the complex field amplitude and $\hat{\mathbf{u}}$ the complex polarization unit vector. Within the dipole approximation, the light-atom interaction is given by

$$V = -\mathbf{E}\cdot\mathbf{d} = -\frac{1}{2}\mathcal{E}\hat{\mathbf{u}}\cdot\mathbf{d}e^{-i\omega t} - \frac{1}{2}\mathcal{E}^{*}\hat{\mathbf{u}}^{*}\cdot\mathbf{d}e^{i\omega t} \tag{4}$$

where $\mathbf{d}$ is the electric dipole operator. Application of Floquet perturbation theory [32] yields the second-order dynamic light shift of an atomic energy level $|a\rangle$ due to a far-off-resonance light field [21]

$$\delta E_a = -\frac{1}{4\hbar}|\mathcal{E}|^2 \sum_b \mathrm{Re}\left\{ \frac{|\langle b|\,\hat{\mathbf{u}}\cdot\mathbf{d}\,|a\rangle|^2}{\omega_{ba} - \omega - i\gamma_{ba}/2} + \frac{|\langle a|\,\hat{\mathbf{u}}\cdot\mathbf{d}\,|b\rangle|^2}{\omega_{ba} + \omega + i\gamma_{ba}/2} \right\} \tag{5}$$

where $|a\rangle$ and $|b\rangle$ are stationary atomic eigenstates with unperturbed energies $E_a = \hbar\omega_a$ and $E_b = \hbar\omega_b$ and spontaneous decay rates γ_a and γ_b, respectively. Here $\omega_{ba} = \omega_b - \omega_a$ is the atomic transition frequency and $\gamma_{ba} = \gamma_b + \gamma_a$ is the transition linewidth. The light shift δE_a can be written as the expectation value $\langle a|V^{\mathrm{ls}}|a\rangle$ of the following operator, cast in spherical

tensor components [21, 31, 32]

$$\begin{aligned} V^{\rm ls} &= V^s + V^v + V^T \\ &= -\frac{1}{4}|\mathcal{E}|^2\Bigg(\alpha_F^s - i\alpha_F^v \frac{[\hat{\mathbf{u}}^* \times \hat{\mathbf{u}}]\cdot \mathbf{F}}{2F} \\ &+ \alpha_F^T \frac{3[(\hat{\mathbf{u}}^*\cdot\mathbf{F})(\hat{\mathbf{u}}\cdot\mathbf{F}) + (\hat{\mathbf{u}}\cdot\mathbf{F})(\hat{\mathbf{u}}^*\cdot\mathbf{F})] - 2\mathbf{F}^2}{2F(2F-1)}\Bigg) \end{aligned} \tag{6}$$

where V^s, V^v and V^T correspond to the scalar, vector and tensor light shifts, respectively, with

$$\alpha_F^s = \frac{1}{\sqrt{3(2F+1)}}\alpha_F^{(0)} \tag{7a}$$

$$\alpha_F^v = -\sqrt{\frac{2F}{(F+1)(2F+1)}}\alpha_F^{(1)} \tag{7b}$$

$$\alpha_F^T = \sqrt{\frac{2F(2F-1)}{3(F+1)(2F+1)(2F+3)}}\alpha_F^{(2)} \tag{7c}$$

being the conventional scalar, vector and tensor polarizabilities of the hyperfine level $|nJF\rangle$, and $\alpha_F^{(K)}$ is the reduced polarizability for the $K = 0, 1, 2$ spherical tensor component. The reduced polarizabilities of hyperfine levels are related to those of their fine structure level through the following identity [31]

$$\alpha_F^{(K)} = (-1)^{I+J+F+K}(2F+1)\begin{Bmatrix} J & F & I \\ F & J & K \end{Bmatrix}\alpha_{nJ}^{(K)} \tag{8}$$

where $\left\{ \begin{smallmatrix} J & F & I \\ F & J & K \end{smallmatrix} \right\}$ denotes the Wigner 6-j symbol and $\alpha_{nJ}^{(K)}$ are the reduced polarizabilities for the fine-structure level $|nJ\rangle$ [21]. The exact form of $\alpha_{nJ}^{(K)}$ is provided in the Supplemental Information. The polarizabilities $\alpha_{nJ}^{(K)}$ can be evaluated using the 'Alkali Rydberg Calculator' or ARC 3.0 Python package [33], where particular attention must be paid to express them in the reduced form utilized in Eq. (8).

Here we comment on the roles of the scalar, vector[34] and tensor light shifts in shaping the potential experienced by the atom in sublevel $|FM\rangle$. From Eqs. (6) and (7) it is clear that the scalar shift V^s is independent of Zeeman sublevel but differs for hyperfine states of different F. The vector shift V^v involves mixing between sublevels of different M, introducing a state-dependency to the potential that is proportional to the ellipticity of the field through $[\hat{\mathbf{u}}^* \times \hat{\mathbf{u}}]$. For linearly polarized light this cross product, and hence the vector shift, vanishes,

leaving only V^s and V^T. The tensor shift V^T does not vanish, in general, under linear polarization and cannot be neglected, but for alkali-metal atoms in the ground state $nS_{1/2}$, $J = 1/2$ and therefore $\alpha_F^T = 0$ [21]. In such a scenario, the absence of V^v and V^T ensures that the total light shift is state-independent. For excited states such as $nP_{3/2}$, $J = 3/2$ and $\alpha_F^T \neq 0$, then V^T introduces a state-dependency even under linear polarization, though this contribution is typically small with respect to the scalar and vector shifts.

2. Surface-interaction potential

Atoms located near the surface of a waveguide experience an attractive potential that is expressed with a surface-interaction operator. If one assumes that this surface-interaction potential is invariant with sublevel $|FM\rangle$, but not with fine structure level $|nJ\rangle$, then this operator is diagonal in the hfs basis,

$$V^{\text{surf}} = U_{\text{surf}} \mathbb{1} \tag{9}$$

where U_{surf} is the surface-interaction potential. We approximate U_{surf} as the non-retarded van der Waals potential for a planar surface [12]

$$U_{\text{surf}}^{\text{vdW}} = -\frac{C_3}{d_a^3} \tag{10}$$

where d_a is the normal atom-surface separation and C_3 is a constant that depends on atomic species and surface permittivity. At a given distance, usually for $d_a > \lambda_0/2\pi$ (where λ_0 is an atom-specific transition wavelength), the surface potential takes on the Casimir-Polder form $U_{\text{surf}}^{\text{CP}} = -C_4/d_a^4$. By approximating the surface potential everywhere with the van der Waals form, our simulations slightly overestimate the atom–surface attraction at distances far away from the waveguide, leading to conservative estimates of the trap depth and location. Finally, we determine the total trapping potential $U_{\text{trap}}(\mathbf{r})$ by diagonalizing the total interaction Hamiltonian $\bar{H}^{\text{int}}$ of Eq. (2) at each spatial location $\mathbf{r} = (x, y, z)$ to obtain a set of eigenstates and their corresponding eigenenergies. The eigenenergies define the trapping potential U_{trap} experienced by the atom in each of the Zeeman sublevels $|FM\rangle$, where $F \in \{|I - J|, \ldots, I + J\}$ and $M \in \{-F, \ldots, F\}$, such that the Hamiltonian $\bar{H}^{\text{int}}$ has dimension $(2F + 1)$.

B. State-insensitive trap on a waveguide

1. *Waveguide eigenmodes*

Here, we use a two-color 'magic compensation' scheme [12, 13, 35] to engineer a state-insensitive trap for Cs atoms in the evanescent region above a ridge nanowaveguide. We consider an optical ridge waveguide that is infinitely long with width $W = 500$ nm and height $H = 200$ nm, made of silicon nitride (Si_3N_4) atop a silicon dioxide (SiO_2) bottom cladding (Fig. 1). This waveguide supports eigenmodes of the form of Eq. (3) with frequency ω and field envelope

$$\boldsymbol{\mathcal{E}}^{\pm}(\mathbf{r}) = \begin{pmatrix} \mathcal{E}_x(x,y) \\ \mathcal{E}_y(x,y) \\ \pm i\mathcal{E}_z(x,y) \end{pmatrix} e^{\pm i\beta z} \tag{11}$$

for real $\mathcal{E}_{\{x,y,z\}}$. Here, $\pm$ denotes forward/backward propagation along the z-axis (along the waveguide) and β denotes the propagation constant of the eigenmode, which encodes the full modal dispersion of the waveguide geometry. At the operating wavelengths considered here, Si_3N_4 and SiO_2 are non-absorbing and β is real; in general it differs from the bulk value $n\omega/c$ of the waveguide. The eigenmodes and their propagation constants are determined numerically [36], for which we enforce the normalisation condition [17]

$$2\epsilon_0 \int d\mathbf{r}\, \epsilon(\mathbf{r}) \left|\boldsymbol{\mathcal{E}}^{\pm}(\mathbf{r})\right|^2 = \hbar\omega \tag{12}$$

where ϵ_0 is the vacuum permittivity and $\epsilon(\mathbf{r})$ the relative permittivity at location $\mathbf{r}$. The eigenmodes of ridge and rib waveguides are well understood in the context of atomic trapping [16, 37, 38]. The fundamental TM_{00} eigenmodes are well suited for deep atomic traps thanks to the large intensity and long decay length in the evanescent electric field above the waveguide, as shown in Fig. 2(a) and (b).

The $\pm\pi/2$ phase difference between transverse and longitudinal components follows from the transversality of Maxwell's equations, which requires the axial field component to satisfy $E_z = \pm i/\beta \times (\nabla_\perp \cdot \boldsymbol{\mathcal{E}}^{\pm}_\perp) \equiv \pm i\mathcal{E}_z$, where $\perp$ denotes the transverse coordinates. Consequently, the polarization vector of the eigenmodes traces out an ellipse in propagation along z, which flips handedness upon reversal of the propagation direction. This ellipticity is strongest in regions of sharp field gradients i.e. near the waveguide surface, leading to a significant state-dependency in the trapping potential due to the vector shift. Noting that $|\hat{\mathbf{u}}^* \times \hat{\mathbf{u}}| =$

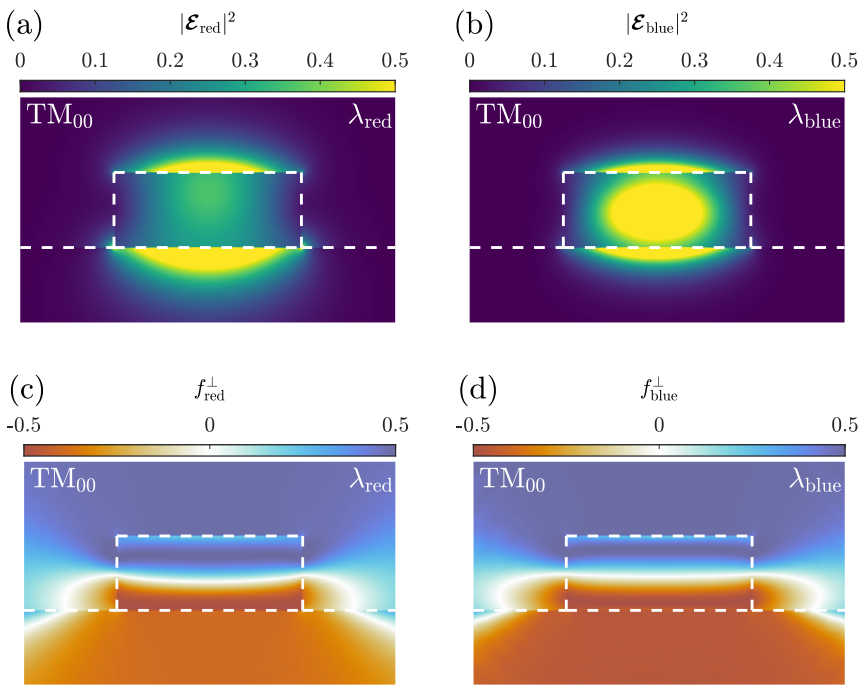


FIG. 2. Normalised optical intensities of the $\rm TM_{00}$ modes at the (a) red-detuned and (b) blue-detuned magic wavelengths (saturated color scale). The long evanescent tails of the $\rm TM_{00}$ modes make them amenable for atom trapping. Panels (c) and (d) show the corresponding transverse field polarization factors $f^{\perp}_{\rm red}$ and $f^{\perp}_{\rm blue}$, respectively.

$2\mathcal{E}_z\mathcal{E}_\perp/|\mathcal{E}^{\pm}|^2$ where $\mathcal{E}_\perp$ is the transverse field magnitude, the ratio of the vector to scalar light shifts is written

$$\left|\frac{U^v}{U^s}\right| \sim \frac{\alpha^{(1)}}{\alpha^{(0)}} \times \frac{\mathcal{E}_z\mathcal{E}_\perp}{|\mathcal{E}^{\pm}|^2} = \frac{\alpha^{(1)}}{\alpha^{(0)}} \times f^{\perp} \tag{13}$$

where $f^{\perp} = \mathcal{E}_z\mathcal{E}_\perp/|\mathcal{E}^{\pm}|^2$ is the transverse field polarization factor [17]. This quantifies the local ellipticity of the eigenmodes and reaches its maximum value of $f^{\perp} \approx 0.5$ for the $\rm TM_{00}$ modes in the evanescent region above the waveguide, as shown in Fig. 2(c) and (d).

Atoms are typically trapped near nanostructures using a two-color scheme [8, 37, 39]. Red- and blue-detuned modes, defined relative to the $\rm D_1$ and $\rm D_2$ lines, provide attractive and repulsive potentials respectively, for which an appropriate choice of power ratio $P_{\rm red}/P_{\rm blue}$ generates a stable, time-independent trap in the evanescent region. For a single pair of red- and blue-detuned modes, this potential provides transverse confinement of atoms but allows for free propagation down the waveguide axis, and is thus deemed an 'atom guide' [37, 39]. To enable probing of the internal state of an atom within the two-color potential, one

can select magic wavelengths for the red- and blue-detuned modes. Magic wavelengths correspond to zero differential light shift between states [24, 40], such that atoms in either state experience an identical light shift and near-identical trapping. This quality has been leveraged to measure internal state populations and perform state-selective spectroscopy of both cesium [13] and strontium [14] atoms trapped along optical nanofibers.

Here, we choose Cs and its magic wavelengths for the $6S_{1/2}$ and $6P_{3/2}$ states (and select the excited state hyperfine level of $F' = 4$), but note that any atomic species possessing a pair of red- and blue-detuned magic wavelengths is suitable. To ensure that U_{trap} is of a similar shape and depth for all $|F'M'\rangle$ sublevels, we assumed linearly polarized light but included the tensor shift in our computations. We then averaged these wavelengths over $|M'| = 0, \ldots, 4$ to yield $\lambda_{\text{red}} = 935.0$ nm and $\lambda_{\text{blue}} = 685.5$ nm. Further details of our computation are provided in the Supplemental Information, including simulations of the differential light shift. Both wavelengths are sufficiently long to support guided TM_{00} eigenmodes, yet the longer red mode carries a larger proportion of its total energy flux in the evanescent region compared to the blue mode, as shown by the mode shapes in Fig. 2(a) and (b).

2. Magic compensated optical lattice

While a single pair of propagating red- and blue-detuned modes provide transverse confinement, they do not provide axial confinement. Axial confinement can be achieved with an additional counter-propagating red-detuned mode, which corrugates the potential along the waveguide to realize a periodic optical lattice. Atoms are confined in three-dimensions at the antinodes of the lattice, as depicted in Fig. 1. For a pair of counter-propagating red-detuned modes with envelopes given by Eq. (11) and with equal frequencies $\omega_r^+ = \omega_r^- \equiv \omega_r$ and propagation constants $\beta_r^+ = \beta_r^- \equiv \beta_r$, the resulting standing wave is linearly polarized everywhere in space,

$$\boldsymbol{\mathcal{E}}_{\text{red}}^{\text{SW}} = \boldsymbol{\mathcal{E}}_{\text{red}}^{+} + \boldsymbol{\mathcal{E}}_{\text{red}}^{-} = \begin{pmatrix} 2\mathcal{E}_{x,r}\cos(\beta_r z) \\ 2\mathcal{E}_{y,r}\cos(\beta_r z) \\ -2\mathcal{E}_{z,r}\sin(\beta_r z) \end{pmatrix}, \tag{14}$$

for which the corresponding polarization vector $\hat{\mathbf{u}}_{\text{red}}$ satisfies $[\hat{\mathbf{u}}_{\text{red}}^* \times \hat{\mathbf{u}}_{\text{red}}] = 0$ such that $V_r^v = 0$ (zero red vector shift). The red-detuned modes with spatial period $2\pi/\beta_r$ produce an

attractive, axially periodic potential with spatial period π/β_r, and the traveling blue-detuned mode produces the smooth repulsive potential to complete the optical trap. We emphasize again that the red standing wave contributes zero vector shift, whereas *any additional single-beam modes*, such as the single traveling blue mode here, will render the optical lattice state-dependent. This non-zero blue mode ellipticity is shown in Fig. 2(d), resulting in a vector shift $V_b^v \neq 0$.

To cancel the blue vector shift, we apply the 'magic compensation' scheme [12, 13] to our ridge waveguide geometry and introduce an additional counter-propagating blue-detuned mode. Our blue-detuned modes are mutually detuned with respect to the blue magic frequency $\omega_b = 2\pi c/\lambda_{\text{blue}} = \omega_{\text{D}_2} + \Delta\omega_b$, where ω_{D_2} is the D_2 transition frequency. We have $\omega_b^+ = \omega_b + \delta\omega_b^\pm/2$ and $\omega_b^- = \omega_b - \delta\omega_b^\pm/2$, where the *blue two-photon detuning* $\delta\omega_b^\pm = \omega_b^+ - \omega_b^-$ is introduced to avoid a standing wave pattern in the blue-detuned field with spatial period $2\pi/\beta_b$ [12]. The magnitude of this two-photon detuning is selected to be much larger than the characteristic trap frequency, $\delta\omega_b^\pm \gg \omega_{\text{trap}}$, which is typically $O(10^2 - 10^3)$ kHz for waveguide-based traps [13, 14, 17]. This ensures that the beat pattern between the two blue-detuned fields oscillates much faster than the atomic motion and is therefore averaged out over motional timescales (see the Supplementary Information for a justification). Assuming $\boldsymbol{\mathcal{E}}_b^{+*} \approx \boldsymbol{\mathcal{E}}_b^-$, the total blue-detuned vector shift is $V_b^v \propto \alpha_F^v(\omega_b^+) - \alpha_F^v(\omega_b^-)$, which to first order in $1/\Delta\omega_b$ becomes [12]

$$\alpha_F^v(\omega_b^+) - \alpha_F^v(\omega_b^-) \sim -\frac{2\delta\omega_b^\pm}{\Delta\omega_b^2} + O\left(\frac{1}{\Delta\omega_b^3}\right). \tag{15}$$

For our blue detuning $\Delta\omega_b/2\pi \approx 85$ THz, selecting $\delta\omega_b^\pm/2\pi = O(10^1)$ GHz yields $\frac{\delta\omega_b^\pm}{\Delta\omega_b} \sim 1 \times 10^{-5}$. The blue-detuned vector shift is therefore *non-zero*, but remains significantly smaller than scalar and tensor shifts; the magnitude of this vector shift could be tuned by $\Delta\omega_b$, though we do not address this degree of freedom in this work. Due to the ∼GHz two-photon detuning, each blue-detuned mode contributes an axially smooth, repulsive potential to the total light shift. It follows then that the total light shift operator of the interaction Hamiltonian in Eq. (2) is

$$V^{\text{ls}} = V_r^{\text{ls}} + V_b^{\text{ls},+} + V_b^{\text{ls},-} \tag{16}$$

where V_r^{ls} and $V_b^{\text{ls},\pm}$ are the operators for the red-detuned standing wave and blue-detuned forward/backward modes, respectively. Note that we have neglected interference between the red- and blue-detuned fields due to their large mutual detuning [22].

We provide simulations of our state-insensitive two-color optical lattice in Figs. 3 and 4. We define x relative to the waveguide center and shift the vertical coordinate so that $y = 0$ coincides with the top edge of the waveguide. Atoms are trapped in the evanescent region $|x| < W/2$ and $y > 0$. To compute the surface potential in the evanescent region, we determined the van der Waals constants C_3 of Eq. (10) for the $6S_{1/2}$ and $6P_{3/2}$ states of Cs near a Si_3N_4 surface. This was carried out numerically with ARC [33] which for an atom in state $|a\rangle$ calculates

$$C_3 = \frac{1}{4\pi\epsilon_0} \sum_b \frac{n(\omega_{ab})^2 - 1}{n(\omega_{ab})^2 + 1} \cdot \frac{\left|d_x^{ab}\right|^2 + \left|d_y^{ab}\right|^2 + 2\left|d_z^{ab}\right|^2}{16} \tag{17}$$

where $n(\omega_{ab})$ is the refractive index of Si_3N_4 evaluated at the transition frequency [41] ω_{ab}, and $d^{ab}_{\{x,y,z\}}$ are the components of dipole matrix element $\mathbf{d}^{ab}$. Our calculated values are $C_3(6S_{1/2})/h = 1.5$ kHz µm^3 and $C_3(6P_{3/2})/h = 1.8$ kHz µm^3, respectively. In general, the depth of an optical trap is proportional to the local electric field intensity and hence to the power carried by the guided mode. For the two red-detuned modes we chose $P_{\text{red}} = 2{\times}2$ mW, and the blue-detuned modes were supplied with $P_{\text{blue}} = 2 \times 23$ mW, giving a total input power of $P_{\text{tot}} = 50$ mW through the ridge waveguide. Lastly, we select the blue two-photon detuning $\delta\omega_b^{\pm}/2\pi = 3$ GHz.

The resulting trapping potential in the transverse plane for all ground $|F = 4, M\rangle$ and excited state $|F' = 4, M'\rangle$ sublevels is shown in Fig. 3. The trapping potential $U_{\text{trap}}(6S_{1/2}\,|F = 4, M = 0\rangle)$ in the evanescent region is at its deepest at the trapping location $\mathbf{r} = \mathbf{r}_{\text{trap}}$ (Fig. 3(a)). An atom at $\mathbf{r} = \mathbf{r}_{\text{trap}}$ experiences a quadratic potential along both the x- and y-directions (Fig. 3(b) and (c)), which correspond to extreme trap depths $|U_x| \approx 1.27$ mK and $|U_y| \approx 2.21$ mK, respectively, for the $6S_{1/2}\,|FM\rangle$ sublevels. Note that the non-zero vector shift between the $6S_{1/2}\,|FM\rangle$ sublevels is not visible at this scale, but is of order $O(10^1 - 10^2)$ nK depending on position along each axis. The weakest trap direction occurs along the ζ line in Fig. 3(a), which connects the symmetrically distributed saddle points to $\mathbf{r}_{\text{trap}}$. A quadratic potential is also formed along the ζ direction, as shown in Fig. 3(d), corresponding to a true trap depth in the transverse plane $|U_\zeta| \approx 0.55$ mK for the $6S_{1/2}\,|FM\rangle$ sublevels. The non-zero tensor light shift of the $6P_{3/2}\,|F'M'\rangle$ sublevels has caused a ~ 500 µK splitting in the potential. However, this splitting is not sufficiently large to disrupt the trapping, such that atoms may be probed within the lattice without suffering ejection.

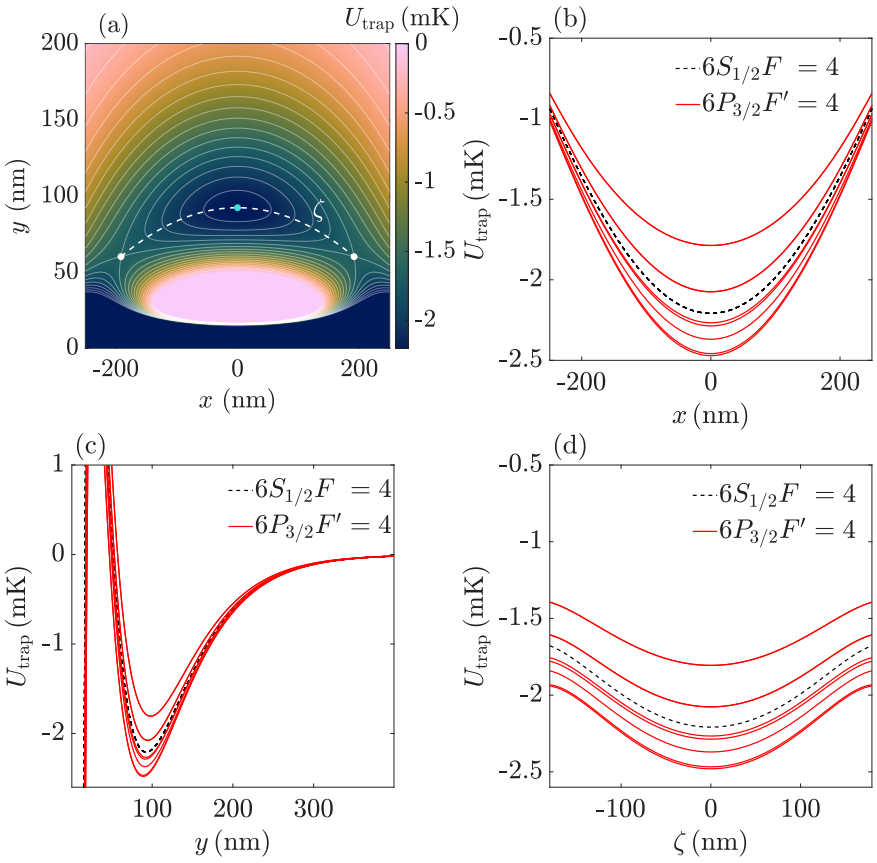


FIG. 3. Transverse dependence of the two-color trapping potential for $z = 0$. (a) $U_{\rm trap}$ for the $6S_{1/2}\,|F = 4, M = 0\rangle$ ground state sublevel. The dashed line represents the weakest trap direction, labeled ζ, which connects the local minimum (blue) to the saddle points (white). $U_{\rm trap}$ for all $6S_{1/2}\,|F + 4, M\rangle$ and $6P_{3/2}\,|F' = 4, M'\rangle$ sublevels along the (b) x-axis at $y = y_{\rm trap}$, (c) the y-axis at $x = x_{\rm trap}$ and (d) the path ζ.

Likewise, the longitudinal trapping potential is provided in Fig. 4. The potential $U_{\rm trap}(6S_{1/2}\,|F = 4, M = 0\rangle)$ is shown in the $x-z$ plane at $y = y_{\rm trap}$ (Fig. 4(a)) and in the $y-z$ plane at $x = x_{\rm trap}$ (Fig. 4(b)), revealing a corrugated potential of period $\pi/\beta_r = 290$ nm. The quadratic potential formed around each antinode of the lattice, as shown in Fig. 4(c) for all $|FM\rangle$ and $|F'M'\rangle$ sublevels, corresponds to a depth $|U_z| \approx 1.83$ mK for the $6S_{1/2}\,|FM\rangle$ sublevels. Atoms are confined longitudinally at the periodic lattice antinodes of coordinates $z_{\rm trap} = m\pi/\beta_r$, where $m \in \mathbb{Z}$ numbers the lattice sites. Figure. 4(d) depicts a close-up of the potential at a lattice antinode, for which a small separation between ground state sublevels is now visible. As in the transverse case (Fig. 3), the $6P_{3/2}\,|F'M'\rangle$ sublevels have an observed ~ 500 µK split with respect to the ground state potential, but again provide a

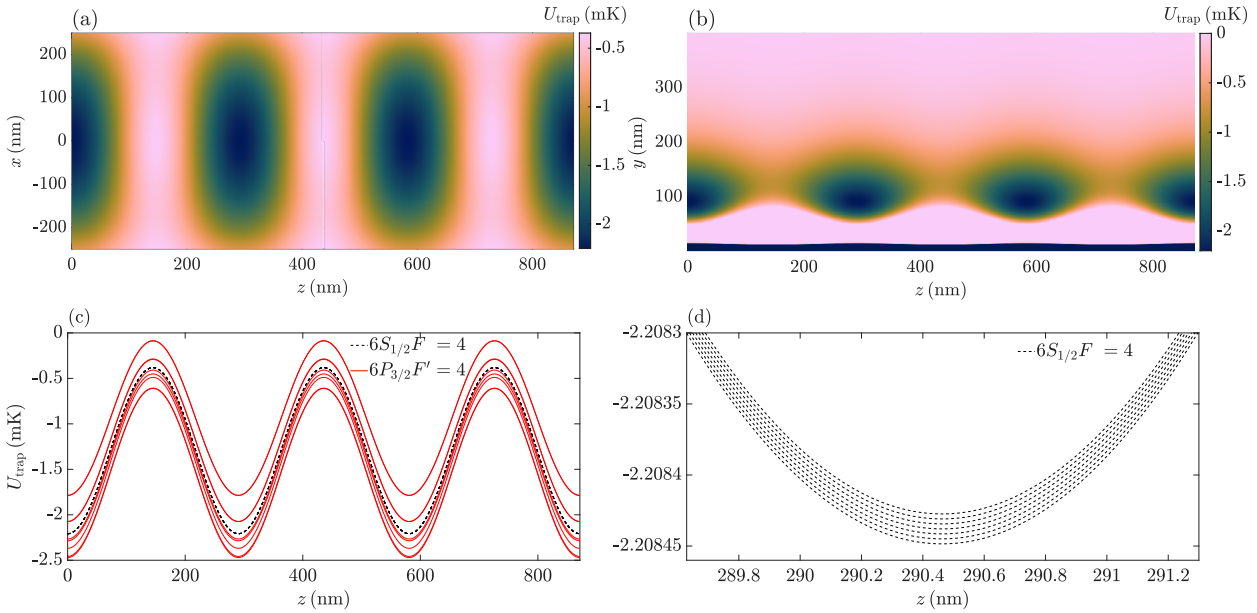


FIG. 4. Longitudinal dependence of the two-color trapping potential. U_{trap} for the $6S_{1/2}\,|F = 4, M = 0\rangle$ ground state sublevel in (a) the $x - z$ plane at $y = y_{\mathrm{trap}}$ and (b) the $y - z$ plane at $x = x_{\mathrm{trap}}$. U_{trap} for all $6S_{1/2}\,|F + 4, M\rangle$ and $6P_{3/2}\,|F' = 4, M'\rangle$ sublevels along the (c) z-axis at $(x = x_{\mathrm{trap}}, y = y_{\mathrm{trap}})$ and (d) a zoomed-in view of panel (c) around an antinode of the lattice potential, for which the splitting between the $|F = 4, M\rangle$ sublevels is now visible.

robust confinement, creating a *state-independent 3D atomic trap* that allows for probing at the D_2 transition.

Beyond providing a ∼mK trap depth indicative of robust atomic confinement, the two-color magic compensated scheme also offers long trap lifetimes and spin-wave coherence times, making the optical lattice suitable for long-duration experiments. The upper limit of the trap lifetime is set by recoil-heating and is estimated as [11]

$$\tau_{\mathrm{rec}} = (T_{\mathrm{trap}} - T_{\mathrm{Cs}})/(T_{\mathrm{rec}}\Gamma_{\mathrm{sc}}) \tag{18}$$

where $\Gamma_{\mathrm{sc}} \approx 147\ \mathrm{s}^{-1}$ is the scattering rate, $T_{\mathrm{trap}} \approx 550$ µK the trap depth along the ζ direction, $T_{\mathrm{Cs}} \approx 30$ µK the assumed temperature of the atoms upon trapping, and $T_{\mathrm{rec}} \approx 198$ nK is the Cs recoil temperature [42], giving $\tau_{\mathrm{rec}} \approx 18$ s. The total scattering rate was calculated as the sum of the red- and blue-detuned rates via the approximation [43] $\Gamma_{\mathrm{sc}} = \Gamma/\Delta\hbar \cdot U_{\mathrm{trap}}(\mathbf{r}_{\mathrm{trap}})$. This recoil-heating estimate is comparable to that reported for nanofiber-based two-color traps [9, 13], though should be regarded as an idealized upper bound. In practice, experimentally measured trap lifetimes in two-color traps are limited

to $\tau \sim O(10^2)$ ms due to fluctuations in phase, polarization and intensity, which cause heating [10, 13]. We estimate the spin-wave coherence time by evaluating the spread in energy shifts arising from the non-zero ellipticity of the interfering blue-detuned fields [12]. The trap frequencies were determined by fitting a harmonic potential to $U_{\mathrm{trap}}(\mathbf{r}_{\mathrm{trap}})$ along the directions $\eta \in \{x, y, z, \zeta\}$, yielding frequencies $(\nu_x, \nu_y, \nu_z, \nu_\zeta) = (267, 1332, 807, 266)$ kHz. For a Cs atom in the motional ground state of the harmonic potential, the motional half-width is $\sigma_\eta = \sqrt{\hbar/2m_{\mathrm{Cs}}\omega_\eta}$, giving $\sigma_\zeta \approx 12$ nm along the most weakly confined direction ζ. Displacing the atom by σ_ζ along ζ yields a differential shift $\delta U_\zeta \approx 21$ nK or $\delta\nu_\zeta \approx 400$ Hz. Thus, the estimated spin-wave coherence time is $\tau_{\mathrm{coh}} = 1/\delta\nu_\zeta = 2.5$ ms. Notably, this quoted value is $O(10^3)$ times greater than coherence times observed in traditional, uncompensated two-color trapping schemes, where ellipticity-induced dephasing is present. Hence, a state-insensitive and three-dimensional optical trap with long trap lifetime and spin-wave coherence time is achieved on a ridge nanowaveguide using a magic compensated scheme, paving the route towards on-chip atomic measurements and devices.

C. State-insensitive atomic conveyor belt

While static optical lattices have been employed for trapping atoms at specific spatial locations, adiabatically ramping the frequency difference between the red-detuned modes causes the lattice to translate backwards or forwards along the waveguide. This enables the micromanipulation of atoms into different waveguide sections or even distinct photonic environments, whilst preserving the coherence of atomic ensembles. Such frequency ramping constitutes an optical conveyor belt [25], which has been demonstrated using guided modes along optical nanofibers [10]. It also shares similarities with optical tractor beam effects [11], though relies on light sources at both waveguide ends. Operating the conveyor effect with our magic compensated scheme offers substantially longer spin-wave coherent transport distances than with an uncompensated scheme, for which we assume a spin-wave coherence time of only 5 µs. At a lattice speed of $v = 0.5$ cm/s, the corresponding coherent transport distance is only $d_{\mathrm{coh}} = v \times \tau_{\mathrm{coh}} = 25$ nm, a prohibitively short distance for applications (which may require coherent transport distances to µm scales). Here, we report that our magic compensated conveyor belt yields spin-wave coherent transport distances that are approximately 500 times longer.

1. Conveyor effect

To realize a controllable moving optical lattice for coherent atomic transport at lattice speed v, we adapt our static magic compensated scheme described above by introducing a red two-photon detuning $\delta\omega_r^{\pm}$, which is distinct from the blue two-photon detuning $\delta\omega_b^{\pm}$. The red two-photon detuning is required to be of $O(10^0 - 10^2)$ kHz ($\delta\omega_r^{\pm} \ll \omega_r$), such that the frequency of the two red-detuned counter-propagating modes is $\omega_r^{\pm} = \omega_r \pm \delta\omega_r^{\pm}/2 \approx \omega_r$. In this regime, the propagation constants and field amplitudes are almost identical, ($\beta_r^{+} \approx \beta_r^{-} = \beta_r$ and $\mathcal{E}_\eta^{+} \approx \mathcal{E}_\eta^{-} = \mathcal{E}_\eta$), allowing the total red-detuned field to be approximated as a moving monochromatic standing wave of frequency ω_r, with positive-frequency envelope

$$\boldsymbol{\mathcal{E}}_{\mathrm{red}}^{\mathrm{SW}}(t) = \begin{pmatrix} 2\mathcal{E}_x \cos\left(\beta z - \delta\omega_{\mathrm{red}}^{\pm} t/2\right) \\ 2\mathcal{E}_y \cos\left(\beta z - \delta\omega_{\mathrm{red}}^{\pm} t/2\right) \\ -2\mathcal{E}_z \sin\left(\beta z - \delta\omega_{\mathrm{red}}^{\pm} t/2\right) \end{pmatrix}. \tag{19}$$

This field remains linearly polarized everywhere along the waveguide with zero ellipticity (and hence zero vector shift), and moves at velocity $\mathbf{v} = (\delta\omega_r^{\pm}/2\beta_r)\,\hat{\mathbf{z}}$ along the axial direction.

We compute the moving lattice potential for all ground and excited state sublevels using the full light shift operator of Eq. (6), now with time-dependent amplitude $\mathcal{E}_r(t)$ and polarization $\hat{\mathbf{u}}_r(t)$ for the red-detuned light. This moving standing wave approximation results from the bichromatic optical Bloch equations, as shown in the Supplementary Information. Our new scheme produces an optical lattice identical to the static case described above, which now translates at velocity $\mathbf{v}$ along the waveguide, as shown in Fig. 5(a). Trapped atomic ensembles remain in a coherent state as the potential remains state-insensitive even under propagation. Thus, atoms are delivered along a 'magic conveyor belt' along the waveguide. In Fig. 5(a), we set the red two-photon detuning to $\delta\omega_r^{\pm}/2\pi = 18$ kHz, giving a lattice speed of $v \approx 0.5$ cm/s. The potential $U_{\mathrm{trap}}(x_{\mathrm{trap}}, y_{\mathrm{trap}})$ is plotted along the waveguide over three spatial lattice periods $3\pi/\beta_r$ at increasing time increments up to one time period $T_l = 2\pi/\delta\omega_r^{\pm} = 55.56$ µs. Naturally, the trapping potentials of all ground and excited state sublevels translate in-phase and retain fixed amplitude, thus enabling the resonant probing of trapped atoms at the D_2 transition without risking ejection.

Lastly, using the spin-wave coherence time in the compensated scheme of $\tau_{\mathrm{coh}} = 2.5$ ms, the spin-wave coherent transport distance for the 'magic conveyor belt' is calculated to

be $d_{\mathrm{coh}} = 12.5$ µm, which is 500 times greater than the $d_{\mathrm{coh}} = 25$ nm estimated for an uncompensated scheme. An atomic ensemble remains phase-stable over translations up to ≈ 40 lattice sites, thus enabling the delivery of a prepared atomic ensemble to regions far away from the initial trapping site.

2. Accelerator effect

Finally, we leverage the 'magic conveyor belt' to design an atom accelerator. Inspired by the tractor beam accelerator effect along a nanofibre [11], our conveyor effect can be used to accelerate atoms to a desired velocity, then release them to propagate freely along the waveguide axis in a state-insensitive trap potential (see Fig. 5(b)). Atoms are first captured in the stationary, magic compensated two-color lattice. Then, we slowly increase the red two-photon detuning to adiabatically accelerate both the lattice and its trapped atoms to a target velocity $\mathbf{v}$. Once the target velocity is reached, the red-detuned standing wave is gradually ramped off, eliminating the moving optical lattice. A pair of *additional* counter-propagating red-detuned modes, mutually detuned by ~ 3 GHz around the magic frequency ω_r, are simultaneously ramped on at the same rate. Note that the total power in the red-detuned compensated pair must be selected so as to ensure an approximately constant transverse depth. This preserves the trapping potential in the transverse plane whilst transforming the longitudinal potential from a standing wave to a flat atom guide. Atoms then freely propagate at an average velocity of $\mathbf{v}$ down the waveguide.

In simulation, a linear ramp rate was chosen to ramp off/on the red-detuned standing wave/magic compensated pair. We selected a ramping time equal to one lattice period $T_{\mathrm{ramp}} = T_l = 55.56$ μs in order to adiabatically transition the atoms from the conveyor belt to the flat atom guide. Note that experimentally, one can achieve ramping on/off times of the order of $T_{\mathrm{ramp}} < 100$ ns [11]. In Fig. 5(b), the ramping is shown to relax the standing wave form at $t = 0$ to the atom guide potential at $t = T_l$, thus allowing for free propagation at times $t > T_l$. Note that we depict only the power-ramping sequence of the accelerator effect in Fig. 5(b), as the procedure for increasing the lattice velocity is standard [25]. The new ingredient here is the 'double compensated' atom guide, which maintains state-insensitivity after the ramping sequence.

We stress here the new contribution this work makes towards the optical transport of

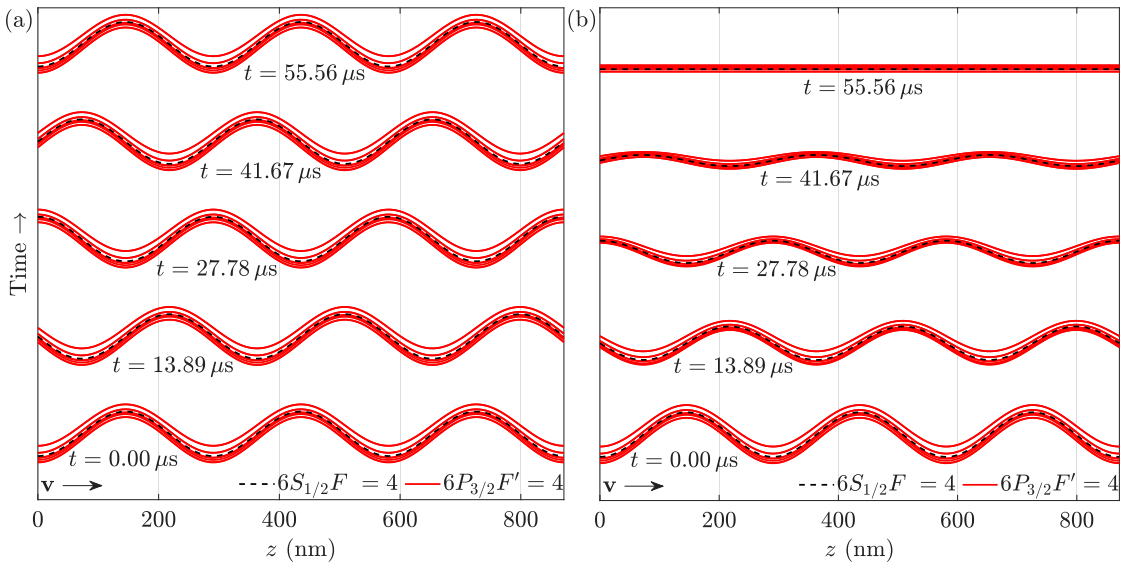


FIG. 5. State-insensitive (a) conveyor and (b) accelerator effects. $U_{\rm trap}(x_{\rm trap}, y_{\rm trap})$ simulated along the z-axis over one optical period $T_l = 55.56$ µs, where velocity $\mathbf{v}$ labels the propagation direction. The ramping time in (b) was selected as $T_{\rm ramp} = T_l$.

atoms along nanostructures. So far previous work has largely focused on ground state atom transport, mainly along optical nanofibers [10, 11], neglecting the complex polarization structure of the fiber eigenmodes. This is often done by approximating the Stark shift with the scalar term $V^s = -1/4 \cdot |\mathcal{E}|^2 \alpha_F^s$, which is a valid approximation for linearly polarized light. At the vicinity of nanofibers, nanowaveguides and any other surface, the evanescent field breaks down this approximation. Here, we model the light-atom interaction with the full light-shift operator of Eq. (6), and develop a state-insensitive conveyor belt that transports atoms in all ground and excited state sublevels simultaneously. This allows for the measurement of both ground and excited state populations during the atom motion without incurring ejection losses. Finally, our magic conveyor belt scheme is a decisive step towards realizing efficient, long-distance transport of coherently prepared atomic ensembles across photonic environments, and the basis for developing further state-insensitive quantum devices, such as accelerometers and interferometers.

III. DISCUSSION

In summary, we have designed a state-insensitive optical lattice and 'magic conveyor belt' for guiding cold atoms along a ridge nanowaveguide, suitable for integrated photonic platforms and on-chip quantum technology devices. The photonic nanostructure enables extreme optical trap depths of ~ 1 mK at total operating powers below 50 mW, relaxing the cooling requirements of the atomic ensemble to $\mathcal{O}(10^1)$ µK. We further develop an state-insensitive atom conveyor scheme that supports simultaneous transport of atoms in all ground and excited state Zeeman sublevels, thus enabling coherence-preserving transport of pre-prepared atomic ensembles, and unlike previously reported schemes allows for non-destructive measurements, as the moving atoms can be probed at the D_2 line without incurring atom ejection from the conveyor. Furthermore, we demonstrate an accelerator effect for the atoms, with a tunable mechanism for selecting atom velocities in propagation along the waveguide, which can enable the controlled atom injection into a matter wave interferometer. Finally, the simplistic ridge waveguide geometry considered here, means that this state-insensitive magic conveyor scheme is fairly general and broadly applicable to other waveguide and nanophotonic geometries, and well suited to all applications requiring controlled, coherence-preserving atom transport on-chip, paving the way for on-chip quantum technology devices.

---

[1] B. Seaman, M. Krämer, D. Anderson, and M. Holland, Atomtronics: Ultracold-atom analogs of electronic devices, Physical Review A—Atomic, Molecular, and Optical Physics **75**, 023615 (2007).

[2] L. Amico, D. Anderson, M. Boshier, J.-P. Brantut, L.-C. Kwek, A. Minguzzi, and W. von Klitzing, Colloquium: Atomtronic circuits: From many-body physics to quantum technologies, Reviews of Modern Physics **94**, 041001 (2022).

[3] J. Polo, W. J. Chetcuti, E. C. Domanti, P. Kitson, A. Osterloh, F. Perciavalle, V. P. Singh, and L. Amico, Perspective on new implementations of atomtronic circuits, Quantum Science and Technology **9**, 030501 (2024).

[4] Y. B. Ovchinnikov, A perspective on integrated atomo-photonic waveguide circuits, Applied Physics Letters **120** (2022).

[5] C. Ryu and M. G. Boshier, Integrated coherent matter wave circuits, New Journal of Physics **17**, 092002 (2015).

[6] A. Orozco, W. Kindel, N. Karl, Y.-Y. Jau, M. Gehl, G. Biedermann, and J. Lee, A sub-5mw evanescent field atom guide with nanofibers towards guided atom interferometry with membrane waveguides, arXiv preprint arXiv:2311.07055 (2023).

[7] V. Balykin, K. Hakuta, F. Le Kien, J. Liang, and M. Morinaga, Atom trapping and guiding with a subwavelength-diameter optical fiber, Physical Review A—Atomic, Molecular, and Optical Physics **70**, 011401 (2004).

[8] F. Le Kien, V. I. Balykin, and K. Hakuta, State-insensitive trapping and guiding of cesium atoms using a two-color evanescent field around a subwavelength-diameter fiber, Journal of the Physical Society of Japan **74**, 910 (2005).

[9] E. Vetsch, D. Reitz, G. Sagué, R. Schmidt, S. T. Dawkins, and A. Rauschenbeutel, Optical interface created by laser-cooled atoms trapped in the evanescent field surrounding an optical nanofiber, Physical review letters **104**, 203603 (2010).

[10] P. Schneeweiss, S. T. Dawkins, R. Mitsch, D. Reitz, E. Vetsch, and A. Rauschenbeutel, A nanofiber-based optical conveyor belt for cold atoms, Applied Physics B **110**, 279 (2013).

[11] M. Sadgrove, S. Wimberger, and S. Nic Chormaic, Quantum coherent tractor beam effect for atoms trapped near a nanowaveguide, Scientific reports **6**, 28905 (2016).

[12] C. Lacroûte, K. Choi, A. Goban, D. Alton, D. Ding, N. Stern, and H. J. Kimble, A state-insensitive, compensated nanofiber trap, New Journal of Physics **14**, 023056 (2012).

[13] A. Goban, K. Choi, D. Alton, D. Ding, C. Lacroûte, M. Pototschnig, T. Thiele, N. Stern, and H. J. Kimble, Demonstration of a state-insensitive, compensated nanofiber trap, Physical review letters **109**, 033603 (2012).

[14] G. Kestler, K. Ton, D. Filin, C. Cheung, P. Schneeweiss, T. Hoinkes, J. Volz, M. Safronova, A. Rauschenbeutel, and J. Barreiro, State-insensitive trapping of alkaline-earth atoms in a nanofiber-based optical dipole trap, PRX Quantum **4**, 040308 (2023).

[15] V. A. Pivovarov, A. S. Sheremet, L. V. Gerasimov, J. Laurat, and D. V. Kupriyanov, Quantum interface between light and a one-dimensional atomic system, Physical Review A **101**, 053858 (2020).

[16] Y. B. Ovchinnikov and F. E. Ayi-Yovo, Towards all-optical atom chips based on optical waveguides, New Journal of Physics **22**, 053003 (2020).

[17] T.-H. Chang, B. M. Fields, M. E. Kim, and C.-L. Hung, Microring resonators on a suspended membrane circuit for atom–light interactions, Optica **6**, 1203 (2019).

[18] R. Guo, Q. He, Z. Zhang, Y. Xu, S. Zhang, Q. Lang, S. Xiao, P. Han, J. Wang, T. Ding, *et al.*, High-q silicon microring resonator with ultrathin sub-wavelength thicknesses for sensitive gas sensing, Applied Physics Reviews **11** (2024).

[19] X. Zhou, H. Tamura, T.-H. Chang, and C.-L. Hung, Trapped atoms and superradiance on an integrated nanophotonic microring circuit, Physical Review X **14**, 031004 (2024).

[20] L. Amico, G. Birkl, M. Boshier, and L.-C. Kwek, Focus on atomtronics-enabled quantum technologies, New Journal of Physics **19**, 020201 (2017).

[21] F. Le Kien, P. Schneeweiss, and A. Rauschenbeutel, Dynamical polarizability of atoms in arbitrary light fields: general theory and application to cesium, The European Physical Journal D **67**, 92 (2013).

[22] F. Le Kien, P. Schneeweiss, and A. Rauschenbeutel, State-dependent potentials in a nanofiber-based two-color trap for cold atoms, Physical Review A—Atomic, Molecular, and Optical Physics **88**, 033840 (2013).

[23] J. McKeever, J. Buck, A. Boozer, A. Kuzmich, H.-C. Nägerl, D. Stamper-Kurn, and H. J. Kimble, State-insensitive cooling and trapping of single atoms in an optical cavity, Physical review letters **90**, 133602 (2003).

[24] J. Ye, H. J. Kimble, and H. Katori, Quantum state engineering and precision metrology using state-insensitive light traps, science **320**, 1734 (2008).

[25] D. Schrader, S. Kuhr, W. Alt, M. Müller, V. Gomer, and D. Meschede, An optical conveyor belt for single neutral atoms, Applied Physics B **73**, 819 (2001).

[26] Y. Miroshnychenko, W. Alt, I. Dotsenko, L. Förster, M. Khudaverdyan, D. Meschede, D. Schrader, and A. Rauschenbeutel, An atom-sorting machine, Nature **442**, 151 (2006).

[27] M. E. Kim, T.-H. Chang, B. M. Fields, C.-A. Chen, and C.-L. Hung, Trapping single atoms on a nanophotonic circuit with configurable tweezer lattices, Nature communications **10**, 1647 (2019).

[28] L. Xu, L.-X. Wang, G.-J. Chen, L. Chen, Y.-H. Yang, X.-B. Xu, A. Liu, C.-F. Li, G.-C. Guo, C.-L. Zou, *et al.*, Transporting cold atoms towards a gan-on-sapphire chip via an optical conveyor belt, Chinese Physics Letters **40**, 093701 (2023).

[29] L. Zhou, A. Graf, and G. Raithel, Sagnac tractor atom interferometer on photonic integrated circuit, arXiv preprint arXiv:2511.05405 (2025).

[30] F. Gu, S. G. Menon, D. Maier, A. Das, T. Chakraborty, W. Tittel, H. Bernien, and J. Borregaard, Hybrid quantum repeaters with ensemble-based quantum memories and single-spin photon transducers, npj Quantum Information **11**, 182 (2025).

[31] P. Rosenbusch, S. Ghezali, V. Dzuba, V. Flambaum, K. Beloy, and A. Derevianko, ac stark shift of the cs microwave atomic clock transitions, Physical Review A—Atomic, Molecular, and Optical Physics **79**, 013404 (2009).

[32] K. Beloy, *Theory of the ac stark effect on the atomic hyperfine structure and applications to microwave atomic clocks* (University of Nevada, Reno, 2009).

[33] E. J. Robertson, N. Šibalić, R. M. Potvliege, and M. P. Jones, Arc 3.0: An expanded python toolbox for atomic physics calculations, Computer Physics Communications **261**, 107814 (2021).

[34] The vector shift is often cast in terms of a fictitious magnetic field of the form $\mathbf{B}^{\rm fict} \propto i[\hat{\mathbf{u}}^* \times \hat{\mathbf{u}}]$. See Refs. 21 and 22.

[35] D. Ding, A. Goban, K. Choi, and H. J. Kimble, Corrections to our results for optical nanofiber traps in cesium, arXiv preprint arXiv:1212.4941 (2012).

[36] *COMSOL Multiphysics® v. 6.2*, COMSOL AB, Stockholm, Sweden.

[37] A. Barnett, S. Smith, M. Olshanii, K. Johnson, A. Adams, and M. Prentiss, Substrate-based atom waveguide using guided two-color evanescent light fields, Physical Review A **61**, 023608 (2000).

[38] T. H. Stievater, D. A. Kozak, M. W. Pruessner, R. Mahon, D. Park, W. S. Rabinovich, and F. K. Fatemi, Modal characterization of nanophotonic waveguides for atom trapping, Optical Materials Express **6**, 3826 (2016).

[39] Y. B. Ovchinnikov, S. Shul'Ga, and V. Balykin, An atomic trap based on evanescent light waves, Journal of Physics B: Atomic, Molecular and Optical Physics **24**, 3173 (1991).

[40] B. Arora, M. Safronova, and C. W. Clark, Magic wavelengths for the np-ns transitions in alkali-metal atoms, Physical Review A—Atomic, Molecular, and Optical Physics **76**, 052509 (2007).

[41] K. Luke, Y. Okawachi, M. R. Lamont, A. L. Gaeta, and M. Lipson, Broadband mid-infrared frequency comb generation in a si3n4 microresonator, Optics letters **40**, 4823 (2015).

[42] D. A. Steck, Cesium d line data, (2003).

[43] R. Grimm, M. Weidemüller, and Y. B. Ovchinnikov, Optical dipole traps for neutral atoms, in *Advances in atomic, molecular, and optical physics*, Vol. 42 (Elsevier, 2000) pp. 95–170.

ACKNOWLEDGMENTS

The authors are grateful to Matt Jamieson and Anaïs Dorne for helpful discussions.

FUNDING

All authors acknowledge funding from EPSRC Grant No. EP\X012689\1. A.D. gratefully acknowledges support from the Royal Society University Research Fellowship Grant Nos. URF\R1\180097 and URF\R\231024, Royal Society Research Grant No. RGS\R1\211093, funding from EPSRC Grant No. EP\Y008774\1, and funding from EPSRC for the CDT in Topological Design Grant No. EP\S02297X\1. D.J.P. acknowledges funding from the Royal Academy of Engineering Chair in Emerging Technologies CiET 2021/123.

DATA AVAILABILITY

The data featured in all figures of the main- and supplementary-texts is available upon reasonable request from the corresponding author.

CODE AVAILABILITY

The code used to simulate all results quoted in the main- and supplementary-texts is available upon reasonable request from the corresponding author.

AUTHOR CONTRIBUTIONS

H.J.P. conceived the state-insensitive conveyor scheme, developed all code, carried out all simulations, and drafted the manuscript and supplementary information. P.F.G. and D.J.P. contributed to the waveguide design and discussions on the trapping method. M.S. contributed to the design of the waveguide geometry and materials. A.D. contributed to

the development of the trapping scheme, discussions on its applications, and the numerical simulations, and contributed to the development of the manuscript. All authors contributed to editing the manuscript.

COMPETING INTERESTS

The authors declare no competing interests.

Supplementary Files

This is a list of supplementary files associated with this preprint. Click to download.

- StateInsensitiveConveyorSubmissionSI.pdf